Published online 26 February 2018

Nucleic Acids Research, 2018, Vol. 46, No. 6 ***3103–3118***
doi: 10.1093/nar/gky125

Investigation of sliding DNA clamp dynamics by single-molecule fluorescence, mass spectrometry and structure-based modeling

Varun V. Gadkari[1,2,†], Sophie R. Harvey[1,3,†], Austin T. Raper[1,2,†], Wen-Ting Chu[4], Jin Wang[4,5,*], Vicki H. Wysocki[1,*] and Zucai Suo[1,2,*]

[1]Department of Chemistry and Biochemistry, The Ohio State University, Columbus, OH 43210, USA, [2]The Ohio State Biochemistry Program, The Ohio State University, Columbus, OH 43210, USA, [3]School of Chemistry, Manchester Institute of Biotechnology, University of Manchester, Manchester M1 7DN, UK, [4]State Key Laboratory of Electroanalytical Chemistry, Changchun Institute of Applied Chemistry, Chinese Academy of Sciences, Changchun, Jilin 130022, P.R. China and [5]Department of Chemistry and Physics, State University of New York at Stony Brook, Stony Brook, NY 11794-3400, USA

Received November 03, 2017; Revised January 23, 2018; Editorial Decision February 09, 2018; Accepted February 12, 2018

ABSTRACT

Proliferating cell nuclear antigen (PCNA) is a trimeric ring-shaped clamp protein that encircles DNA and interacts with many proteins involved in DNA replication and repair. Despite extensive structural work to characterize the monomeric, dimeric, and trimeric forms of PCNA alone and in complex with interacting proteins, no structure of PCNA in a ring-open conformation has been published. Here, we use a multidisciplinary approach, including single-molecule Förster resonance energy transfer (smFRET), native ion mobility-mass spectrometry (IM-MS), and structure-based computational modeling, to explore the conformational dynamics of a model PCNA from *Sulfolobus solfataricus* (*Sso*), an archaeon. We found that *Sso* PCNA samples ring-open and ring-closed conformations even in the absence of its clamp loader complex, replication factor C, and transition to the ring-open conformation is modulated by the ionic strength of the solution. The IM-MS results corroborate the smFRET findings suggesting that PCNA dynamics are maintained in the gas phase and further establishing IM-MS as a reliable strategy to investigate macromolecular motions. Our molecular dynamic simulations agree with the experimental data and reveal that ring-open PCNA often adopts an out-of-plane left-hand geometry. Collectively, these results implore future studies to define the roles of PCNA dynamics in DNA loading and other PCNA-mediated interactions.

INTRODUCTION

In all three domains of life, DNA replication is an intricate, and stringently coordinated process that ensures faithful and efficient copying of genetic material. Such a complicated process is accomplished by a variety of enzymes including DNA polymerases (1–8), glycosylases (9–11), ligases (12,13) and nucleases (14–16), which often interact with an evolutionarily conserved sliding DNA clamp. While encircling duplexed DNA, the sliding DNA clamp functions as a scaffold for DNA replication and repair machinery (17–19). Moreover, sliding DNA clamps have been identified and studied in all domains of life, *e.g.* the β clamp of *Escherichia coli*, the gene 45 protein (gp45) of T4 bacteriophage, and proliferating cell nuclear antigen (PCNA) in yeast, humans, and the archaeon *Sulfolobus solfataricus* (*Sso*) (20,21).

Previous studies have shown that despite low sequence similarity, all sliding DNA clamps share a similar toroidal structure with a central hole to accommodate a DNA duplex (20). Despite the highly conserved ring-shaped structure of DNA sliding clamps, the complexity of their subunit composition varies. For instance, the β clamp of *E. coli* is homodimeric, while PCNA clamps in archaeal and eukaryotic organisms are trimeric (20). Although many PCNA clamps are homotrimeric, *Sso* PCNA is heterotrimeric, consisting of three distinct PCNA monomer subunits: PCNA1, 2, and 3 (21). As a result, proper subunit arrangement, subunit interfaces (22–24), and exclusive subunit binding part-

*To whom correspondence should be addressed. Tel: +1 614 688 3706; Fax: +1 614 292 6773; Email: suo.3@osu.edu
Correspondence may also be addressed to Vicki H. Wysocki. Tel: +1 614 292 8687; Email: wysocki.11@osu.edu
Correspondence may also be addressed to Jin Wang. Tel: +1 631 632 1185; Fax: +1 631 632 7960; Email: jin.wang.1@stonybrook.edu
†These authors contributed equally to this work as first authors.

ners have been identified for *Sso* PCNA1, PCNA2, and PCNA3 (21,24–26). Previous studies have established that formation of the *Sso* PCNA trimer follows a sequential process, which begins with dimerization of PCNA1 and PCNA2, followed by recruitment of PCNA3 to form the heterotrimer (21–24).

While crystal structures exist for each *Sso* PCNA monomer (23), the PCNA1:PCNA2 dimer (23), and the ring-closed PCNA heterotrimer (22–24), no crystal structure is available for the *Sso* PCNA heterotrimer in a ring-open conformation. However, biochemical experiments have shown that the *Sso* PCNA heterotrimer opens at the interface between PCNA1 and PCNA3 in order to be loaded onto DNA by a clamp loading accessory protein, replication factor C (RFC) (27). To date, only the gp45 homotrimer of T4 bacteriophage has been crystallized in a ring-open conformation, but only while in complex with its clamp loader assembly (gp62/gp44 complex) (28). In this structure, the clamp is open out-of-plane and adopts a right-hand geometry, consistent with the right-handed helix of double-stranded DNA (28). Paradoxically, fluorescence studies report that the gp45 DNA clamp exists primarily in a ring-open form while in solution (29), yet only the ring-closed form has been crystallized in the absence of the clamp loader (30). Accordingly, sliding DNA clamps likely undergo conformational dynamics while free in solution, as well as in complex with clamp loaders, DNA, or both.

As sliding DNA clamps serve significant roles in numerous fundamental aspects of DNA metabolism, it is crucial to understand if their conformational dynamics may influence biochemical events. Here, we use a state-of-the-art multidisciplinary approach, including single-molecule Förster resonance energy transfer (smFRET), native ion mobility-mass spectrometry (IM-MS), and structure-based computational modeling, to characterize the dynamics of *Sso* PCNA. Our smFRET results suggest that PCNA exists in dynamic equilibrium between ring-open and ring-closed conformations at the PCNA1:PCNA3 interface, and that ionic strength can modulate the transition kinetics between these states. Moreover, this dynamic open-closed equilibrium of *Sso* PCNA can also be monitored in the gas-phase using IM-MS as demonstrated by two populations of distinct collisional cross sections, which were also sensitive to changes in ionic strength. Finally, structure-based computational modeling of *Sso* PCNA agreed with the experimentally observed two-state system and its dependence on ionic strength. However, in contrast to the ring-open structure of gp45 in complex with its clamp loader, our computational results suggest an unusual out-of-plane ring-opening of PCNA at the PCNA1:PCNA3 interface to mainly adopt left-hand geometry. This result may have general implications for loading and unloading of PCNA to DNA. Taken together, our results demonstrate the dynamics of an evolutionarily conserved sliding DNA clamp, and implore future efforts to understand how PCNA motions may influence protein-protein and protein-DNA interactions.

MATERIALS AND METHODS

Expression and purifications of proteins

Sso PCNA plasmids were obtained as generous gifts from the lab of Dr Stephen D. Bell at Indiana University in Bloomington, IN. Genes coding for *Sso* PCNA1, PCNA2, PCNA3 were expressed by three separate plasmids, while the covalently-linked PCNA heterotrimer (PCNA1–2–3) was expressed as a fusion from a single gene encoding PCNA1, PCNA2, and PCNA3 covalently joined at the PCNA1:PCNA2 and PCNA2:PCNA3 interfaces by amino acid linkers (ASGAGGSEGGGSEGGTSGAT) as described previously (27). To this construct, site-specific S→C mutations were engineered at residues S64 of PCNA1 and S189 of PCNA3 for fluorophore labeling. Additionally, a gene sequence encoding an AviTag peptide (GLNDIFEAQKIEWHE) to allow site-specific biotinylation by BirA (31) and subsequent surface immobilization for smFRET studies was added to the C-terminus of PCNA1–2–3 before the 6xHis tag.

All expression plasmids were individually transformed into *E. coli* strain Rosetta (DE3) and expressed separately using autoinduction in ZYP-5052 medium (32). After growth, cells were harvested (4000 rpm for 20 min), resuspended in Buffer A (50 mM HEPES (pH 8 at 4°C), 100 mM NaCl, and 1 mM DTT), and lysed by French press at 20 000 PSI before clarifying the lysate by ultracentrifugation (40 000 rpm for 40 min). As *Sso* PCNA is thermostable, the clarified lysate was subject to heat shock by incubation at 60°C for 10 min to precipitate contaminating proteins which were subsequently removed by ultracentrifugation (40 000 rpm for 40 min).

Sso PCNA1, PCNA2, and PCNA3 subunits were expressed and purified independently. Each subunit was purified by anion exchange, heparin, and size exclusion chromatography. Briefly, a PCNA subunit was bound to a 5 ml HiTrap Q column (GE Healthcare) and eluted through a linear salt gradient (up to 1 M NaCl). Fractions containing the PCNA monomer were dialyzed against Buffer A, loaded onto a 5 ml HiTrap heparin column (GE Healthcare), and eluted through a linear salt gradient (up to 1 M NaCl). Fractions with negligible nucleic acid contamination (260/280 ratio < 0.6) were dialyzed against Buffer A, concentrated to less than 1 ml, loaded and eluted from a HiPrep 26/60 Sephacryl S-100 column (GE Healthcare). The PCNA heterotrimer was formed by incubating equimolar amounts of purified PCNA1, PCNA2, and PCNA3 at 4°C for 1 h in Buffer A, before purification by size-exclusion chromatography, as described above.

Following heat shock, the covalently-linked PCNA1–2–3 protein was bound to Ni^{2+}-NTA resin (Qiagen) and eluted through a linear imidazole gradient (up to 1 M imidazole) in Buffer A. Following dialysis against Buffer A, the protein was purified by HiTrap heparin and size-exclusion chromatography as described above for the PCNA monomers. The purified PCNA1–2–3 was then biotinylated by following a previously published protocol (31,33) before fluorophore labeling with a 15-fold molar excess of thiol-reactive Cy3- and Cy5-maleimide (Lumiprobe) overnight at 4°C in a buffer containing 50 mM Tris (pH 7.2), 150 mM

NaCl, 0.5 mM TCEP, and 10% glycerol. Free dye was removed by size-exclusion chromatography. The extent of fluorophore labeling was verified by measuring absorbance at 280, 552 and 650 nm for PCNA, Cy3 and Cy5, respectively.

Single molecule measurements

All single-molecule measurements were conducted on a custom built, prism-type total internal reflection microscope, as described previously (34–36). Imaging chambers were assembled from quartz slides and coverslips that were cleaned, passivated, and biotinylated by following a published protocol (34,37). Biotinylated, Cy3-Cy5 labeled PCNA1–2–3 was then surface immobilized following the addition of NeutrAvidin (0.2 mg/ml). After rinsing the imaging chamber with T50 buffer (10 mM Tris–HCl, pH 8.0, 50 mM NaCl) and addition of imaging buffer (50 mM HEPES [pH 7.6], 0.8% w/v D-glucose, 2 mM Trolox, 0.1 mg/ml BSA, 1 mg/ml glucose oxidase, 0.04 mg/ml catalase) containing 0, 250, 500, 750 or 1000 mM NaCl, single-molecule movies were recorded at 25°C using an Andor iXon 897 EM-CCD. Notably, the inclusion of Trolox in the imaging buffer limited acceptor blinking (38). The movies were recorded over several minutes at a reduced laser power and a slow frame rate (2 frames per second) to limit observed rapid photobleaching of Cy3 and Cy5 conjugated to PCNA1–2–3 at higher laser powers.

Single molecule data analysis

Single-molecule movies were processed using IDL (ITT Visual Information Solutions) and custom MATLAB scripts (Center for the Physics of Living Cells, University of Illinois at Urbana-Champaign) to generate traces of donor and acceptor fluorescence intensities for each detected molecule, as previously described (35,36). The traces were subsequently processed and background corrected in MATLAB. Traces showing clear anti-correlated donor and acceptor signals, as well as exhibiting single donor photobleaching events, were selected. FRET efficiency values were calculated as apparent FRET (E_{app}) using Equation (1), where I_D, and I_A are the donor and acceptor fluorescence intensities, respectively.

$$E_{app} = \frac{I_A}{I_D + I_A} \tag{1}$$

For every experiment, FRET efficiency values from >200 FRET trajectories were collected and binned to generate histograms depicting the relative population distributions of FRET events. These data were fit to a sum of Gaussian functions using MATLAB, and percent occupancy of FRET states was calculated as the total area under the individual Gaussian fits. Dwell time analysis was performed as previously described (35,36). Briefly, the duration of each FRET event for the selected molecules was quantified using a thresholding analysis. The 'Low FRET' state was limited by thresholds at FRET efficiencies of 0.2 and 0.65, and the 'High FRET' state was limited by thresholds at FRET efficiencies of 0.65 and 1. The resulting dwell times were compiled to generate survivor functions as previously described (35,36) which were fit to a single exponential decay equation (Equation 2), where $f(t)$ is the fraction of molecules in the designated FRET state after time t, A is the amplitude of the function, and k is the decay rate constant associated with the designated FRET state.

$$f(t) = Ae^{-kt} \tag{2}$$

Mass spectrometry

All mass spectrometry and ion mobility-mass spectrometry studies were performed on an in-house modified Synapt G2 (Waters, Milford, UK) (39). Typical experimental parameters were as follows; capillary voltage of 1.2–1.4 kV, a sampling cone of 20 V, source temperature of 20°C and trap collision energy of 5 V. Gas flows in the trap, helium cell and IM cell were 4, 120 and 60 ml/min respectively. Experimental collisional cross sections were determined using a calibration procedure, with β-lactoglobulin, avidin, concanavilin A, transthyretin and serum amyloid P component as standards (40). In all cases, a trap wave velocity of 250 m/s and height of 3.5 V, ion mobility wave velocity of 300 m/s and height of 17 V, and a transfer wave velocity of 100 m/s and a height of 2 V were used.

Structure-based model

An initial coarse-grained Cα structure-based model (SBM) was generated from the crystal structure of *Sso* heterotrimeric PCNA (PDB 2HII) (chains 1, 2, and 3 contain 249, 243, and 243 amino acids, respectively) (24) using the SMOG on-line toolkit, which included one bead on the Cα atom of each residue of the complex (41–43). The native contact map was built by the Shadow Algorithm (43). Aiming to sample the ring-open conformation of heterotrimeric PCNA, the native contacts between chain 1 and chain 3 were not included in this model. The potential energy function consisted of both bonded and nonbonded terms. Additionally, we introduced charge characterization into our SBM to study the electrostatic interactions in the system. As a result, the potential energy form used in this study is given by the following equation:

$$\begin{aligned} V = & \sum_{bonds} \varepsilon_r (r - r_0)^2 + \sum_{angles} \varepsilon_\theta (\theta - \theta_0)^2 \\ & + \sum_{dihedrals} K_\phi^{(n)} (1 - \cos(n \times (\phi - \phi_0))) \\ & + \sum_{contacts} \varepsilon_{ij} \left(5\left(\frac{\sigma_{ij}}{r_{ij}}\right)^{12} - 6\left(\frac{\sigma_{ij}}{r_{ij}}\right)^{10} \right) \\ & + \sum_{non-contacts} \varepsilon_{NC} \left(\frac{\sigma_{NC}}{r_{ij}}\right)^{12} + V_{Debye-Hückel} \end{aligned} \tag{3}$$

In Equation (3), $\varepsilon_r = 100\varepsilon$, $\varepsilon_\theta = 20\varepsilon$, $K_\phi^{(1)} = \varepsilon$ and $K_\phi^{(3)} = 0.5\varepsilon$. The interaction strength of the Lennard-Jones type potential is proportional to the statistical potential reported for the residue types of i and j by Miyazawa and Jernigan (MJ) (44) to generate the 'flavored model' (45). Therefore, the coefficient of nonbonded contacts, ε_{ij}, is set as follows:

$$\varepsilon_{ij} = \left(\gamma \left(\frac{\varepsilon_{ij}^{MJ}}{\bar{\varepsilon}^{MJ}} - 1 \right) + 1 \right) \tag{4}$$

where ε_{ij}^{MJ} is the original MJ potential, $\bar{\varepsilon}^{MJ}$ is the mean value of the entire set of MJ weights in the complex system,

and γ is set to 1.0 corresponding to the 'flavored model' (45).

The electrostatic interaction is calculated by the Debye–Hückel model, which can quantify the strength of charge-charge attractions and repulsions at various salt concentrations:

$$V_{Debye-Hückel} = \Gamma_{DH} \times K_{coulomb} B(\kappa) \sum_{ij} \frac{q_i q_j \exp(-\kappa r_{ij})}{\varepsilon r_{ij}} \quad (5)$$

In Equation (5), $K_{coulomb} = 4\pi\varepsilon_0 = 138.94$ kJ•mol^{-1}•nm•e^{-2} is the electric conversion factor; $B(\kappa)$ is the salt-dependent coefficient; κ^{-1} is the Debye screening length, which is directly influenced by the salt concentration C_{salt} ($\kappa \approx 3.2\sqrt{C_{salt}}$); ε is dielectric constant, which is set to 80 during the simulations; and Γ_{DH} is the energy scaled coefficient, which aims to make the total energy balanceable. In our model, Lys and Arg residues have a positive point charge (+e) while Asp and Glu have a negative point charge (-e). All charges are placed on the Cα atoms. Besides the systems of variable ionic strengths, there is also a system with no electrostatic interactions. Under physiological ionic strengths ($C_{salt} \sim 0.15$ M), κ is 1.24 nm^{-1}. In our simulations, $\Gamma_{DH} = 0.535$ such that V_{DH} for two oppositely charged atoms located at a distance of 0.5 nm matches the native contact energy. For more details regarding the Debye–Hückel model, the authors cite several helpful publications (46–49).

Molecular dynamics simulations

All molecular dynamic simulations (MD) were performed with Gromacs 4.5.5 (50). In the SBM, reduced units were used in the potentials. Accordingly, the value of simulation temperature is not the same as the 'normal' temperature. To obtain an appropriate simulation temperature, replica-exchange molecular dynamic (REMD) simulations with 24 replicas ranging from about 38 K to 150 K were performed. Each replica was performed for 100 ns. The exchanges were attempted every 5000 steps. As a result, the simulation temperature was set to 85 K. The MD used the Langevin equation with a constant friction coefficient of $\gamma = 1.0$. The cut-off for nonbonded interactions was set to 3.0 nm, and all bonds were constrained using the LINCS algorithm (51). The MD time step was set to 2.0 fs. For thermodynamic simulations, a 1 μs MD simulation was performed on each salt concentration (including 10, 50, 100, 150, 200, 250, 300, and 500 mM, as well as a system without charge interactions). We define that a native contact is formed if the Cα–Cα distance between any given native atom pair is within 1.2× of its native distance. The native distance is calculated from the initial structure model. Therefore, Q_{inter} is defined as the fraction of the interchain native contact number.

Theoretical CCS determination

Theoretical CCS were determined for the C alpha models using the projection approximation (PA) and trajectory method (TJM) models in IMPACT (52), for 50 000 frames in each trajectory. Results were filtered and plotted based on the fraction of native contacts between chain 1 and chain 3 ($Q_{inter13}$) and the ionic strength, where $Q_{inter13} = 0$ represents the open state, $Q_{inter13} = 1$ represents the closed state.

RESULTS

Design of covalently-linked *Sso* PCNA for smFRET

To understand how sliding DNA clamp conformational dynamics may influence biological processes, we sought to first characterize the dynamics of heterotrimeric PCNA from the model organism *Sulfolobus solfataricus*. This well-studied protein consists of three distinct subunits, PCNA1, PCNA2 and PCNA3, serves as a processivity factor during DNA replication, and is implicated as a key component of polymerase switching during translesion DNA synthesis (53–55). Previous studies have revealed that *Sso* PCNA opens at the PCNA1:PCNA3 interface to be loaded onto DNA by RFC (27). However, no crystal structure of PCNA in the ring-open conformation is currently available despite structures of the ring-closed conformation alone (22–24) and in complex with protein binding partners (24–26). Accordingly, we wondered if PCNA maintains an equilibrium between ring-open and ring-closed conformations even in the absence of DNA or RFC. To directly probe for this conformational equilibrium, we designed an inter-subunit FRET construct wherein PCNA1 and PCNA3 were modified with site-specific Cys mutations at S64 and S189, respectively, and were simultaneously labeled with Cy3- and Cy5-maleimide (Figure 1A and B). Based on the crystal structure of *Sso* PCNA, the inter-fluorophore distance in the ring-closed conformation is 45 Å which corresponds to a FRET efficiency of ∼0.80 (Cy3–Cy5 R_0 = ∼54 Å) (56,57). Consequently, conformational transition of *Sso* PCNA from the ring-closed to the ring-open conformation should cause a decrease in FRET efficiency (Figure 1A and B). Notably, while our labeling strategy can result in a heterogeneous population of labeled species (*i.e.* Cy3 at both S64 and S189, Cy5 at both S64 and S189, and single-label species), these molecules do not demonstrate anti-correlated donor and acceptor fluorescence signals during smFRET experiments, and thus were either not observed during smFRET imaging or easily identified for exclusion during data processing. Moreover, the two possible dual-labeled PCNA molecules (i.e. C64–Cy3/C189–Cy5 PCNA and C64–Cy5/C189–Cy3 PCNA) from Cy3–Cy5 labeling are expected to yield equivalent FRET signals during smFRET experiments as each labeling site was carefully selected (i.e. based on the *Sso* PCNA heterotrimer crystal structure, PDB code: 2HII) to avoid secondary structural elements of PCNA while maintaining a high degree of flexibility and solvent accessibility for the conjugated fluorophores. Thus, we assume that the dipole orientation factors (κ^2) (58) for the dual-labeled PCNA molecules with fluorophores positioned at either site should be similar and therefore not affect apparent FRET efficiencies and relative distance changes during our smFRET experiments.

To simplify surface-immobilization for smFRET experiments, PCNA1, PCNA2, and PCNA3 were covalently fused (PCNA1–2–3) through a peptide linker (ASGAG-GSEGGGSEGGTSGAT) between PCNA1 and 2 as well as PCNA2 and 3 (Figure 1C). This same strategy was previously applied to define the single PCNA subunit interface

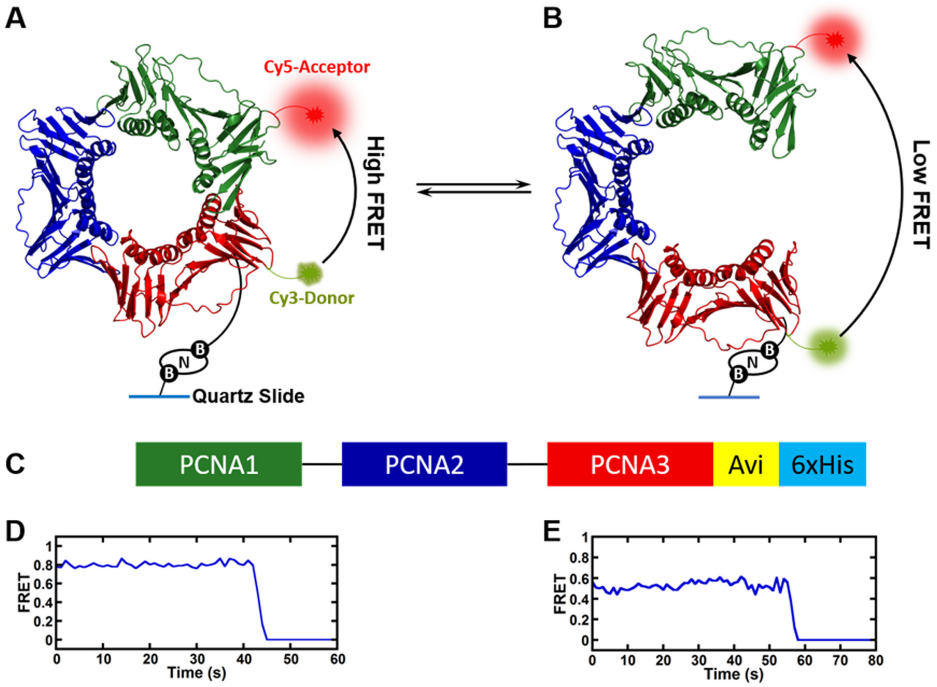

Figure 1. Single-molecule FRET system for Sso PCNA conformational dynamics. (**A**, **B**) Cy3 donor and Cy5 acceptor fluorescent dyes were introduced at the PCNA1:3 interface to probe conformational changes associated with PCNA ring-opening and ring-closing. (**C**) PCNA1–2–3 is covalently-linked at the PCNA1:2, and PCNA2:3 interface. (**D**) Ring-closed PCNA1–2–3 molecules produce high-FRET efficiency signal from 0.60 to 0.90 while (**E**) ring-open PCNA1–2–3 molecules produce low-FRET efficiency signal from 0.40 to 0.60.

(PCNA1:PCNA3) for ring-opening, and this linked construct enhanced DNA polymerase processivity in primer extension assays just as wild-type heterotrimeric PCNA (27). Thus, this covalently-linked PCNA heterotrimer offered the advantage of simplifying the interpretation of smFRET results (i.e. by limiting complicating signals from *in situ* PCNA heterotrimer association and dissociation) to exclusively investigate ring-opening and ring-closing, as well as permitting direct comparison with the previous study (27). To permit wide-field smFRET imaging, we achieved surface immobilization of *Sso* PCNA by engineering a short AviTag (15 amino acid residues) to the C-terminus of the protein to be biotinylated at a specific Lys residue by BirA (31,33). The biotinylated PCNA was then bound by NeutrAvidin which was immobilized to the surface of a quartz microscope slide passivated with biotinylated-PEG molecules. Following surface-immobilization, fluorescence intensity from both donor and acceptor channels was simultaneously recorded during Cy3 excitation with a 532 nm laser. Initial experiments yielded single-molecule trajectories with anti-correlated donor and acceptor signals representing two, non-zero FRET efficiency values near 0.80 (high FRET) and 0.55 (low FRET), which we have attributed to the ring-closed (Figure 1D) and ring-open (Figure 1E) conformations of PCNA, respectively. PCNA was observed to interconvert between the ring-closed and ring-open conformations as demonstrated by FRET fluctuations between the high and low efficiency values (Figure 2) in some single-molecule trajectories. The inclusion of Trolox (2 mM) as an anti-blinking agent in the single-molecule imaging buffer, as well as the anti-correlated signal changes and fluctuations to non-zero FRET efficiency values suggests that the observed FRET transitions do not occur as a result of acceptor blinking (38). However, many single-molecule trajectories demonstrated only high FRET (Figure 1D) or low FRET (Figure 1E) efficiencies until irreversible photobleaching, suggesting that PCNA ring-opening and ring-closing transition kinetics are slow. Accordingly, reversible fluctuations between FRET efficiency states were only occasionally observed (data not shown) before photobleaching during the imaging period of our experiments (~120 s). These results verify the utility of our

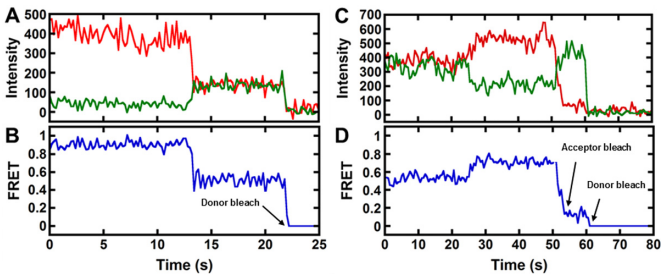

Figure 2. PCNA interconverts between its ring-open and ring-closed conformations. (**A**) Representative donor (green) and acceptor (red) fluorescence trajectories depicting transition from the PCNA ring-closed (high-FRET) to ring-open (low-FRET) conformation before donor photobleaching. (**B**) FRET efficiency trajectory (blue) calculated from the donor and acceptor intensities in (A). (**C**) Representative donor (green) and acceptor (red) fluorescence trajectories depicting transition from the PCNA ring-open (low-FRET) to ring-closed (high-FRET) conformation before acceptor photobleaching. (**D**) FRET efficiency trajectory (blue) calculated from the donor and acceptor intensities in (C).

FRET construct and immobilization strategy, and support the hypothesis that *Sso* PCNA is conformationally dynamic even in the absence of DNA or protein partners.

Investigation of *Sso* PCNA by smFRET

Previous studies have established that the interfaces between each PCNA monomer are partly stabilized by ionic interactions (22–24). Moreover, the interacting regions of PCNA1 and PCNA3 at the PCNA1:PCNA3 interface have clear positive and negative surfaces, respectively (Supplementary Figure S1). We thus wondered if PCNA ring-opening and ring-closing detected through our smFRET methodology (Figures 1 and 2) would be sensitive to the ionic strength of the imaging buffer, which would be observed as changes in the relative distribution of FRET efficiency values and ring-opening/ring-closing transition kinetics upon titration with increasing amounts of NaCl. Accordingly, we performed single-molecule imaging of surface-immobilized, Cy3/Cy5-labeled PCNA1–2–3 in imaging buffer containing different NaCl concentrations (0–1000 mM). Many single-molecule trajectories (>200) at each NaCl concentration were collected and observed FRET efficiencies were binned to generate FRET population distribution histograms (Figure 3). Two FRET populations, corresponding to a high FRET, ring-closed PCNA conformation (E_{app} = 0.7–0.9) and a low FRET, ring-open PCNA conformation (E_{app} = 0.5–0.6) were readily apparent within the FRET distribution histograms (Figure 3A–E). The bimodal FRET distributions were fit to a sum of Gaussian functions in MATLAB to quantify the effect of solution ionic strength on the open-close equilibrium of PCNA. The low- and high-FRET populations (Figure 3A–E, dashed red lines) showed a strong dependence on solution ionic strength as low NaCl concentrations favored the ring-closed PCNA conformation (peak center = 0.80) and high NaCl concentrations favored the ring-open PCNA conformation (peak center = 0.55). In fact, by plotting the relative fraction of low-FRET events against NaCl concentration, a clear linear correlation is apparent as increasing ionic strength presumably disfavors the ring-closed PCNA conformation but favors the ring-open PCNA conformation (Figure 3F). With no NaCl added to the imaging buffer (Figure 3A), a substantial fraction (∼25%) of low-FRET events are still observed in the FRET distribution, suggesting that PCNA ring-opening can still spontaneously occur despite weak shielding of electrostatic interactions. Similarly, at high ionic strength (Figure 3E, 1000 mM NaCl), PCNA ring-closing can still spontaneously occur as ∼25% of molecules remain in the high-FRET, ring-closed conformation despite significant shielding of electrostatic interactions.

To further investigate the conformational dynamics of *Sso* PCNA, we measured the transition kinetics of PCNA ring-opening and ring-closing through a dwell time analysis of our smFRET data at each NaCl concentration. Briefly, we measured the duration of time each molecule spent at a particular FRET efficiency level before transitioning to a different level or photobleaching. Dwell times of PCNA in the ring-closed (i.e. high-FRET) and ring-open (i.e. low-FRET) conformations were binned into histograms which were subsequently integrated, normalized, and inverted to generate survivor functions (Figure 4A, B). Single exponential decay fits to the survivor functions of the high-FRET and low-FRET efficiencies yielded rate constants for PCNA ring-opening (k_{open}) and PCNA ring-closing (k_{close}) at each tested NaCl concentration (Table 1). The value for k_{open} was affected by solution ionic strength. Consistent with the decrease in population of the ring-closed PCNA conformer at increasing ionic strength (Figure 3), k_{open} became more rapid (0.0258–0.130 s^{-1}) as the NaCl concentration was raised from 0 to 1000 mM (Figure 4C and Table 1). In contrast, k_{close} (0.038–0.051 s^{-1}) was not significantly affected by increasing solution ionic strength, suggesting that PCNA ring-closing may occur in two distinct steps, one of which (*i.e.* the protein conformational change associated with ring-closing) is unaffected by solution ionic strength. Consistently, as the solution ionic strength increased, the equilibrium constant (K_{eq}), calculated as k_{open}/k_{close}, also increased thereby reflecting the shift in equilibrium towards the ring-open conformation of PCNA (Table 1). In agreement with the lack of reversible fluctuations between FRET efficiency states before photobleaching in smFRET trajectories, the transition rates measured for ring-opening and ring-closing were indeed small (Table 1). In fact, the time required for all molecules to complete the reaction ($7*t_{1/2}$ = 7*(ln2/k), $t_{1/2}$ = reaction half-life) was 75 s for PCNA opening (i.e. calculated based on average k_{open}) and 109 s for PCNA closing (*i.e.* calculated based on average k_{close}), while photobleaching typically occurred within 120 s during smFRET experiments. As a result, the likelihood of observing both slow ring-opening and slow ring-closing within an individual single-molecule trajectory before donor or acceptor photobleaching was minimal.

Ion mobility-mass spectrometry of *Sso* PCNA

To further probe the conformational dynamics of *Sso* PCNA and support the conclusions of our smFRET analysis, we studied the structure and conformations of *Sso* PCNA by native mass spectrometry (MS). This methodology has been applied to investigate protein-protein interactions in the gas phase as well as to provide low-resolution structural information for proteins and protein complexes, without the need for complicated or potentially disruptive protein labeling (59,60). Coupling nano-electrospray ionization (nESI), a soft ionization technique that preserves noncovalent interactions for transmission into the mass spectrometer (61–63), with ion mobility-mass spectrometry (IM-MS), we can probe protein shape (64,65) and can even observe differences in molecular conformations (66,67).

To verify that subunit fusion did not alter the conformational dynamics of covalently-linked *Sso* PCNA1–2–3 utilized in the smFRET experiments relative to wild-type *Sso* PCNA heterotrimer, we performed native MS on both constructs. For gas phase analysis, each protein was buffer exchanged into a solution consisting of increasing concentrations of 20% triethylammonium acetate (TEAA), and 80% ammonium acetate (AmAc) (100–500 mM mixed acetate salts) to increase ionic strength. We chose to use a combination of AmAc and TEAA as previous studies have shown that TEAA reduces the charge states of the

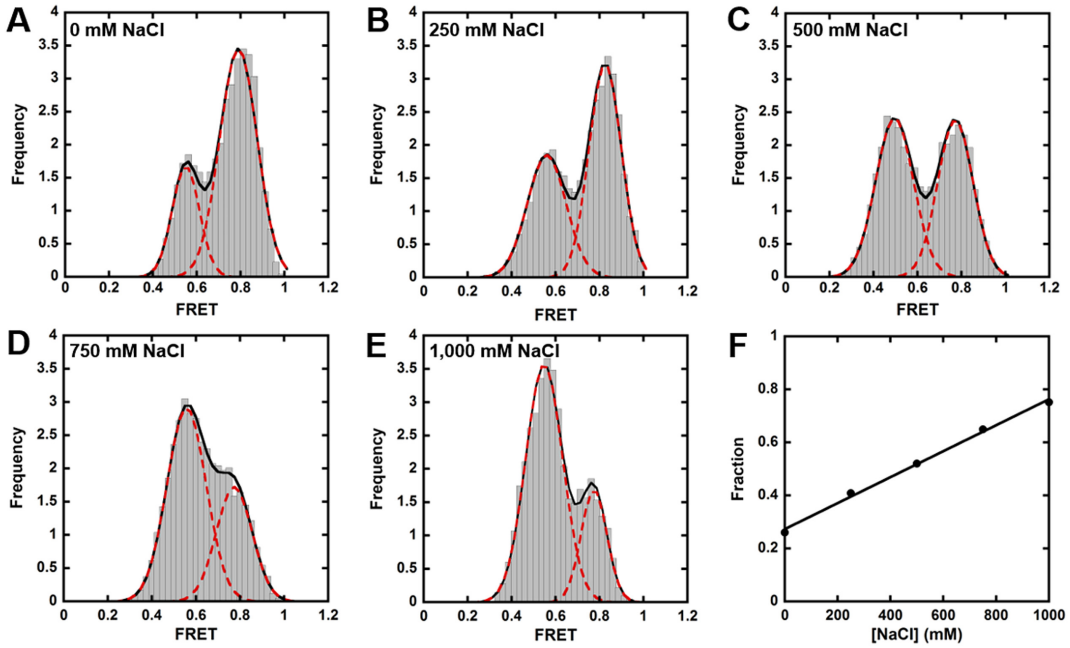

Figure 3. FRET distributions change with increasing NaCl concentrations. FRET trajectories for >200 molecules were compiled and binned to generate FRET distribution histograms for each NaCl concentration, (**A**) 0 mM, (**B**) 250 mM, (**C**) 500 mM, (**D**) 750 mM and (**E**) 1,000 mM NaCl. FRET distribution histograms were fit to a sum of Gaussians function (black line) to extract the individual low-FRET (0.40–0.60) and high-FRET (0.60–0.90) populations (red dashed lines). (**F**) Fraction of PCNA1–2–3 molecules in the ring-open conformation (calculated in A–E) increased linearly as NaCl concentration was increased.

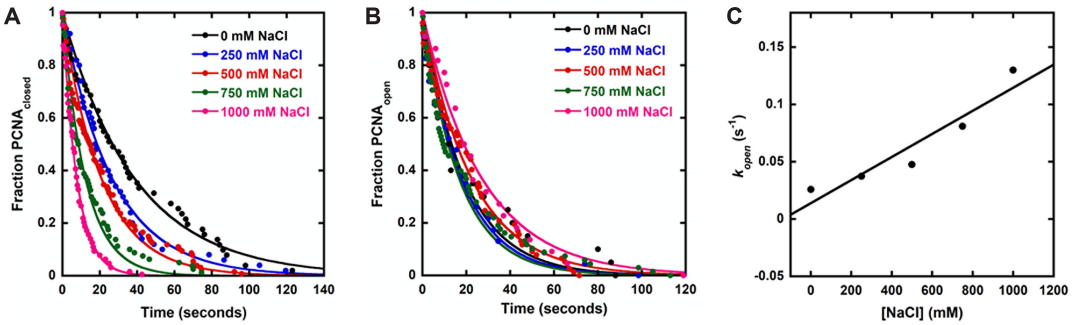

Figure 4. Dwell time analysis of PCNA states. Rates of PCNA (**A**) ring-opening (k_{open}) and (**B**) ring-closing (k_{close}) at each NaCl concentration were extracted by fitting the dwell time survivor functions of the high-FRET and low-FRET states, respectively, to a single exponential decay equation. (**C**) Rates of PCNA ring-opening (k_{open}) were plotted against NaCl concentrations. A linear fit with slope of 1.0×10^{-4} $mM^{-1}s^{-1}$ is shown (black line) to describe the dependence of k_{open} values on NaCl concentrations.

Table 1. Kinetic rates of PCNA ring-opening and ring-closing

NaCl (mM)	k_{open} (s^{-1})[a]	k_{close} (s^{-1})[b]	K_{eq} (k_{open}/k_{close})
0	0.0258 ± 0.0004	0.044 ± 0.004	0.59
250	0.0374 ± 0.0007	0.050 ± 0.002	0.75
500	0.0476 ± 0.0008	0.0405 ± 0.0009	1.18
750	0.081 ± 0.002	0.051 ± 0.002	1.59
1000	0.130 ± 0.002	0.038 ± 0.002	3.42

[a]Dwell time survivor functions to calculate k_{open} (Figure 4A) were generated from smFRET trajectories exhibiting ring-closed→ring-open FRET transitions at 0 (n= 39), 250 (n= 50), 500 (n= 84), 750 (n= 80) and 1000 (n= 64) mM NaCl.
[b]Dwell time survivor functions to calculate k_{close} (Figure 4B) were generated from smFRET trajectories exhibiting ring-open→ring-closed FRET transitions at 0 (n= 20), 250 (n= 23), 500 (n= 77), 750 (n= 68) and 1000 (n= 40) mM NaCl.

protein ions and lower charge states are attributed to a more compact and native-like form of the complex (68,69). While the wild-type PCNA heterotrimer is the predominant species at 100 and 200 mM mixed acetate salts (Figure 5A, B), the mass spectra revealed sample heterogeneity as peaks attributed to monomer and dimer were apparent. The experimental mass for the wild-type PCNA heterotrimer (Figure 5A) was determined to be 82 982 ± 41 Da, which is in good agreement with the theoretical mass (82 395 Da), when adducting of salt and solvent are considered (common in native MS when attempting to keep structures native). Moreover, masses of monomer and dimer were determined to be 27 675 ± 94 Da and 55 393 ± 145 Da, respectively, which are consistent with the theoretical masses (PCNA1: 27 536 Da, PCNA2: 27 436 Da, PCNA3: 27 459 Da, PCNA1+2: 54 972 Da, PCNA2+3: 54 895 Da, PCNA1+3: 54 995 Da). The differences in theoretical masses for the monomer and dimer species are relatively small ($\Delta MW_{(|PCNA1\text{-}PCNA2|)}$ = 100 Da; $\Delta MW_{(|PCNA1\text{-}PCNA3|)}$ = 77 Da; $\Delta MW_{(|PCNA2\text{-}PCNA3|)}$ = 23 Da; $\Delta MW_{(|(PCNA1+2)\text{-}(PCNA2+3)|)}$ = 77 Da; $\Delta MW_{(|(PCNA1+2)\text{-}(PCNA1+3)|)}$ = 23 Da; $\Delta MW_{(|(PCNA1+3)\text{-}(PCNA2+3)|)}$ = 100 Da), corresponding to a theoretical $\Delta m/z$ of 3–14 for the 7+ charge state of the monomer and a theoretical $\Delta m/z$ of 2–9 for the 11+ charge state of the dimer. Accordingly, we cannot confidently assign the identities of the monomer and dimer species present in Figure 5A–C which were acquired using a time-of-flight mass spectrometer and have peak widths (126 and 122, respectively) greater than these theoretical $\Delta m/z$ values. Indeed, given such subtle mass differences, the reported enzyme-catalyzed removal of the N-terminal methionine residue during protein expression in *E. coli*, which occurs with varying efficiency based on protein sequence (70), further complicates assignment of the monomer and dimer species by mass. The higher observed molecular weights in comparison to the theoretical sequences are attributed to the fact that the protein ions will retain salt, solvent, and other adducts during the gentle ionization and desolvation conditions employed here, which were critical for maintaining the native state of the wild-type PCNA heterotrimer (71). However, previous biochemical studies of *Sso* PCNA have reported that only PCNA1 and PCNA2 form a dimer and no homodimerzation of any of the PCNA subunits occurs (21). Hence, the dimer species in our experiments is likely PCNA1+2, while the monomer is PCNA3. The relative intensities of the monomer and dimer species increased at higher ionic strength (Figure 5C, 500 mM) suggesting heterotrimer dissociation as stabilizing electrostatic interactions at the subunit interfaces were presumably shielded. As 500 mM mixed acetate salts resulted in significant decomposition of the heterotrimeric PCNA to monomer or dimer constituents, the wild-type *Sso* PCNA was not analyzed at higher ionic strengths.

As depicted for the dominant charge state (14+), two populations of distinct rotationally averaged collisional cross sections (CCS) of 49 and 52 nm^2 were observed suggesting conformational heterogeneity of heterotrimeric PCNA (Figure 5D–F). As the concentration of mixed acetate salts increased from 100 to 500 mM, the more compact population of ions (i.e. possessing a smaller CCS of ∼49 nm^2) began to diminish while the more extended population of ions (i.e. possessing a larger CCS of ∼52 nm^2) began to increase (Table 2 and Figure 5D–F). These results are consistent with the smFRET data (Figure 3) and suggest that ions with smaller CCS represent the ring-closed conformer of PCNA (discussed in more detail in following sections), which is stabilized at low ionic strength, while ions with larger CCS represent the ring-open conformer of PCNA, which is favored at high ionic strength.

We next examined biotinylated *Sso* PCNA1–2–3 by native IM-MS to better simulate conditions of the smFRET analysis. As expected, the experimental mass of the biotinylated PCNA1–2–3 (Figure 6A) is larger (89 667 ± 103 Da) than wild-type PCNA heterotrimer (82 982 ± 41 Da) which is consistent with the 20 amino acid linkers between PCNA1 and 2 and PCNA2 and 3, as well as the 15 amino acid AviTag conjugated to biotin (total theoretical MW: 88 894 Da). The higher measured molecular weight in comparison to the theoretical is likely due to adducts (such as solvent or salt molecules) remaining on the protein during the ionization and desolvation processes. As with the wild-type PCNA heterotrimer, we systematically increased ionic strength by buffer exchanging aliquots of the biotinylated PCNA1–2–3 into increasing amounts of mixed acetate salts (100–1000 mM) before IM-MS analysis. As expected for a covalent peptide-linked construct, the mass spectra (Figure 6 A – E) obtained at each concentration of mixed acetate salts revealed a homogenous sample of biotinylated PCNA1–2–3 that did not decompose to smaller subunit constituents as ionic strength was increased. The collisional cross section distributions of the two dominant charge states (14+ and 15+) of biotinlylated PCNA1–2–3 (Figure 6F–O) were similar to the wild-type PCNA heterotrimer and revealed two populations of distinct CCS: a compact species at ∼53 nm^2 and an extended species at ∼55 nm^2 (Table 2). Notably, the CCS values for compact and extended biotinylated PCNA1–2–3 were noticeably larger than for wild-type PCNA heterotrimer (∼49 versus ∼53 nm^2 and ∼52 versus ∼55 nm^2, respectively) (Table 2). We attribute these differences in CCS to the 20 amino acid long linkers between PCNA1 and 2 and PCNA2 and 3, as well as the 15 amino acid long AviTag at the protein C-terminus. As with the wild-type PCNA heterotrimer, increasing ionic strength resulted in reduction of the intensity of the compact conformational family and concomitant increase in the intensity of the extended conformational family (Figure 6), which is consistent with the IM-MS data collected for the wild-type PCNA heterotrimer (Figure 5) and indicates that, relative to the wild-type PCNA, neither subunit fusion nor biotinylation of PCNA1–2–3 significantly diminished the ability of the trimer to adopt two distinct conformations. This experimental consistency between the wild-type and covalently-linked constructs verifies the biological relevance of smFRET experiments completed with the covalently-linked PCNA heterotrimer (Figures 1 and 2). We attribute the compact conformational family (Figure 6F–O), at lower CCS, to PCNA1–2–3 in a ring-closed conformation which transitions to an extended ring-open conformation as ionic strength increases. The collisional cross section distributions between the 15+ and 14+ charge states are marginally

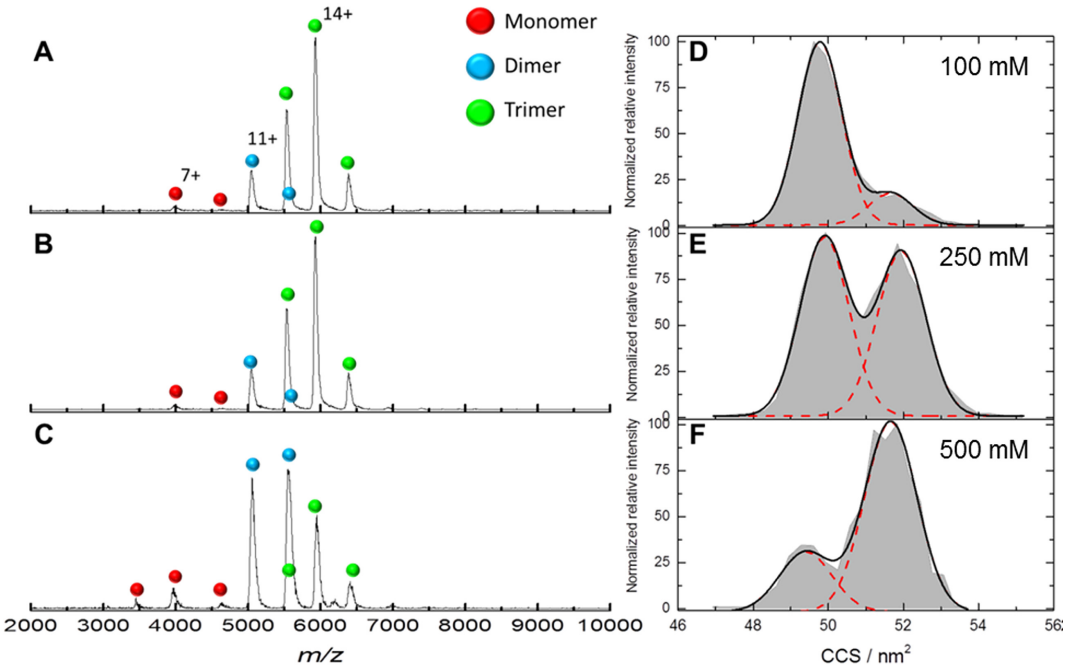

Figure 5. Ion mobility-mass spectrometry of wild-type *Sso* PCNA. Wild-type PCNA trimer was analyzed by IM-MS. Samples were exchanged into buffers containing (**A**) 100, (**B**) 200 and (**C**) 500 mM of 20% triethylammonium acetate (TEAA), and 80% ammonium acetate (AmAc) before introduction to the mass spectrometer by nano-electrospray ionization. Collisional cross section (CCS) distributions for the 14+ charge state of the trimer were obtained from the arrival time distributions using the previously published calibration procedure (40). In (**D**) 100, (**E**) 200 and (**F**) 500 mM mixed acetate salt, the 14+ trimer showed two distributions. The lower CCS distribution is assigned to a ring-closed PCNA trimer, while the higher CCS distribution is expected to be a ring-open form of the PCNA trimer. We observed a transition from the ring-closed to the ring-open PCNA conformation as ionic strength was increased.

Table 2. Collisional cross sections (CCS) in nm^2 for *Sso* PCNA

***14+ charge state*, wild-type PCNA heterotrimer**					
Ionic strength[a,b]	**100 mM**	**200 mM**	**500 mM**		
Ring-closed PCNA	49.7 ± 0.31	49.76 ± 0.46	49.67 ± 0.43		
Ring-open PCNA	51.86 ± 0.44	52.32 ± 1.12	51.96 ± 0.45		
***14+ charge state*, PCNA1–2–3**					
Ionic strength[a,b]	**100 mM**	**250 mM**	**500 mM**	**750 mM**	**1000 mM**
Ring-closed PCNA	52.81 ± 0.15	53.56 ± 0.91	52.77 ± 0.15	52.70 ± 0.39	52.86 ± 0.45
Ring-open PCNA	54.45 ± 0.27	54.59 ± 0.25	54.43 ± 0.09	54.44 ± 0.42	54.50 ± 0.45
***15+ charge state*, PCNA1–2–3**					
Ionic strength[a,b]	**100 mM**	**250 mM**	**500 mM**	**750 mM**	**1000 mM**
Ring-closed PCNA	52.90 ± 0.23	52.81 ± 0.23	53 ± 0.02	53.20 ± 0.38	52.87 ± 0.38
Ring-open PCNA	54.53 ± 0.26	54.55 ± 0.22	54.59 ± 0.10	54.54 ± 0.034	54.66 ± 0.33

[a]Ionic strength results from 80% ammonium acetate, 20% triethylammonium acetate mixture.
[b]Values reported are the average of three different day repeats and the error represents the standard deviation between the three repeats.

different (Figure 6). For example, even at lower concentrations of mixed acetate salts (Figure 6F, 100 mM), the majority of ions at the 15+ charge state adopt the extended ring-open conformation (~55 nm^2), but the minority ring-closed population continues to diminish as ionic strength increases (Figure 6G, H, I, J). This is in contrast to ions of the 14+ charge state which show the majority of ions in the compact ring-closed conformation (52.81 ± 0.15 nm^2) (Figure 6K, 100 mM) prior to increasing ionic strength (Figure 6L–O). This difference with charge state is not unexpected as the more compact population would be expected, on average, to accept fewer charges (*i.e.* smaller charge carrying capacity) during the nano-electrospray ionization process than the more extended population (i.e. larger charge carrying capacity). Hence, we would expect to see a higher population of the compact conformational family in the lower charge states (i.e. 14+) and a higher population of the extended conformational family in the higher charge states (i.e. 15+). Furthermore, while the overall trend observed for the conformational dynamics of biotinylated PCNA1–2–3 at increasing ionic strengths is consistent between the smFRET and IM-MS data, the distributions of PCNA1–2–3 in the ring-open and ring-closed conformations at each salt concentration were slightly different between the two methods. For instance, at concentrations greater than 500 mM NaCl (Figure 3) in the smFRET experiments, the major-

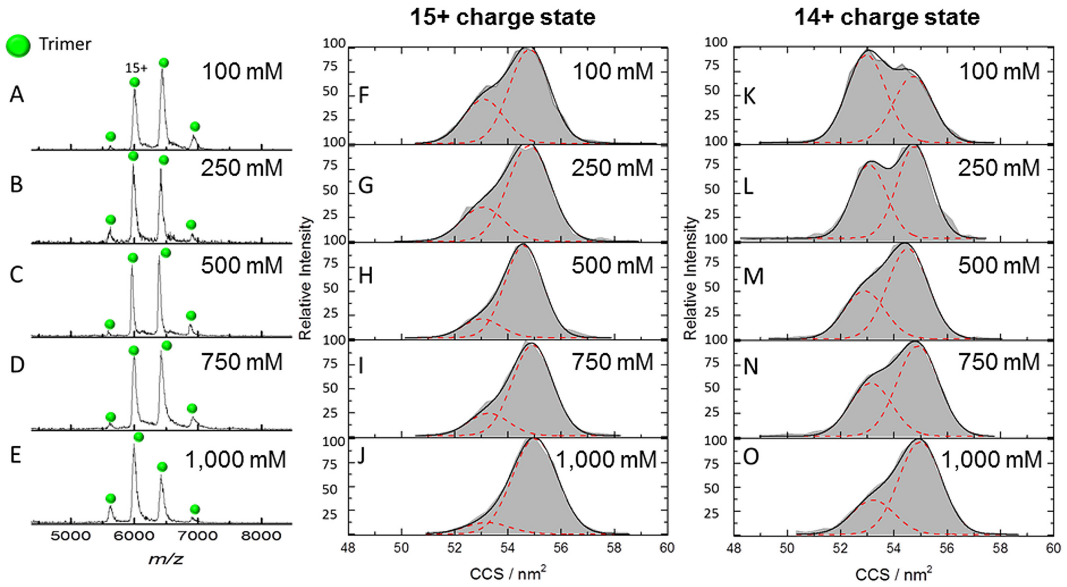

Figure 6. Mass spectrometry of covalently-linked *Sso* PCNA. Biotinylated, covalently-linked PCNA trimer (PCNA1–2–3) was analyzed by mass spectrometry. A mass spectrum is shown for each concentration of 20% triethylammonium acetate (TEAA), and 80% ammonium acetate (AmAc), (**A**) 100, (**B**) 250, (**C**) 500, (**D**) 750 and (**E**) 1000 mM. At all ionic strengths, the dominant species are the 15+ and 14+ charge states of the covalently-linked PCNA trimer. Arrival time distributions were converted to collisional cross section (CCS) distributions, using a previously published calibration procedure (40). CCS distributions of the 15+ charge state are shown for increasing concentrations of mixed acetate salt, (**F**) 100, (**G**) 250, (**H**) 500, (**I**) 750 and (**J**) 1000 mM. CCS distributions of the 14+ charge state are shown for increasing concentrations of mixed acetate salt, (**K**) 100, (**L**) 250, (**M**) 500, (**N**) 750 and (**O**) 1000 mM.

ity of PCNA1–2–3 molecules adopt the ring-open conformation. However, for the 15+ and 14+ charge states of the IM-MS experiments (Figure 6), concentrations of mixed acetate salts as low as 100 (Figure 6F) or 250 mM (Figure 6L), respectively, are sufficient to favor the extended ring-open conformation. Accordingly, as choice of monovalent salt (*i.e.* ammonium acetate versus sodium chloride) did not appreciably influence the smFRET results (Supplementary Figure S2), the observed conformational equilibrium of PCNA may be moderately sensitive to IM-MS processes, such as desolvation and ionization, which may positively contribute to PCNA transitions to the extended, ring-open conformation. Nevertheless, these IM-MS results demonstrate a strong correlation between ionic strength and an extended (ring-open) conformation of PCNA1–2–3, and therefore strongly support the in-solution smFRET data of favorable transitions to a low-FRET, ring-open conformation as solution ionic strength increases (Figure 3). As a result of the wild-type (Figure 5) and covalently-linked (Figure 6) PCNA heterotrimer demonstrating similar dynamic properties during IM-MS analysis, the conformational dynamics of PCNA1–2–3 observed by smFRET (Figure 3) likely emulate those of the wild-type PCNA heterotrimer as well.

Molecular dynamics simulation of *Sso* PCNA

A powerful tool for understanding the mechanisms of protein folding, binding, as well as conformational changes associated with a biological process (72–76) is generation of a structure-based model (SBM). Accordingly, we used the crystal structure of *Sso* PCNA along with our smFRET and IM-MS experimental findings to develop a SBM of PCNA to simulate ring- opening and ring-closing. A coarse-grained SBM consisting of Cα atoms from the wild-type *Sso* PCNA heterotrimer was generated from PDB code 2HII (24). The native contacts between PCNA1 and PCNA3 were omitted from the starting model to allow sampling to the ring-open conformer. Using the *Debye-Hückel* model, a series of long-time (1 μs) molecular dynamic simulations were performed at different ionic strengths (10–500 mM), and the ring-open conformation of the wild-type PCNA heterotrimer was observed at higher ionic strengths. Consistent with the collisional cross section distributions of the wild-type PCNA heterotrimer (Figure 5), our molecular dynamic simulations suggest that the ring-closed conformation of *Sso* PCNA is more stable at lower salt concentrations based on the root-mean-square deviation (RMSD) (Figure 7A) of our SBM with respect to the crystal structure of PCNA in the ring-closed conformation (2HII). Furthermore, the RMSD is shown to increase as the salt concentration is raised from 10 to 500 mM, indicating conformational heterogeneity driven by increased ionic strength (Figure 7A). Our simulation tracked the fraction of native contacts at the PCNA1:PCNA3 interface ($Q_{inter13}$) as ionic strength was increased from 10 to 500 mM (Figure 7B). With *Sso* PCNA in the fully ring-open conformation, $Q_{inter13}$ equals 0, while in the fully ring-closed conformation, $Q_{inter13}$ equals 1, indicating that all native contacts are made. Clearly, the fraction of ring-open PCNA conformers is much lower (i.e. low probability, low $Q_{inter13}$) at low ionic strength, but increases as ionic strength is raised (Figure 7B). Notably, a simulation removing all charge from the system reveals *Sso* PCNA to be in the ring-open conformation as all electrostatic contacts at the PCNA1:PCNA3 interface are eliminated (no

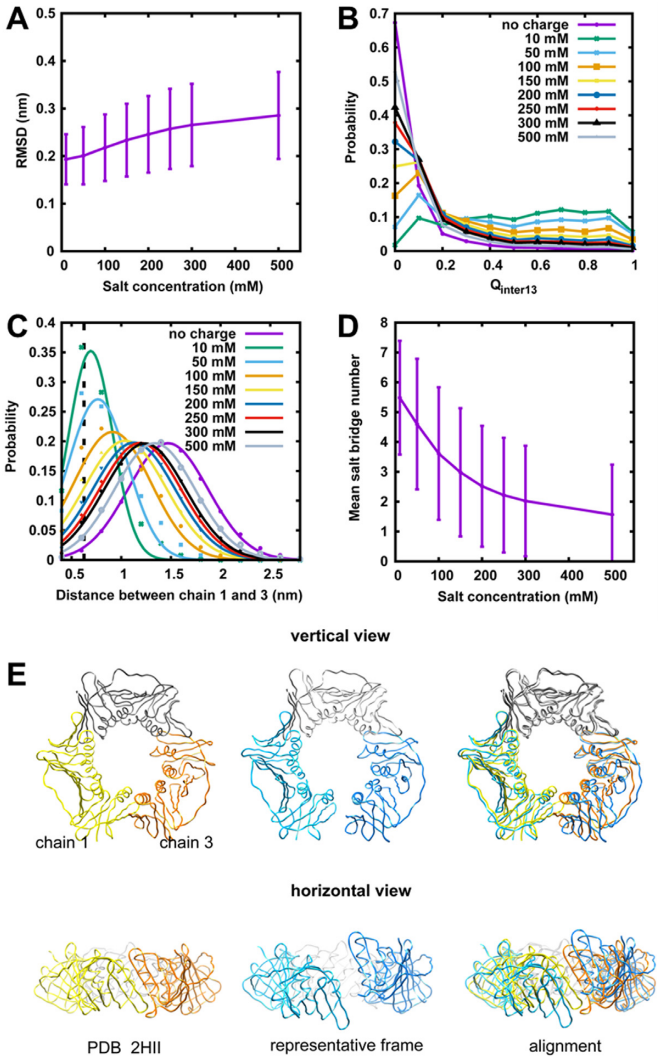

Figure 7. Molecular Dynamic Simulation of the Wild-Type *Sso* PCNA. (**A**) Average RMSD (with standard deviation) of heterotrimeric PCNA at different salt concentrations, with respect to the structure 2HII. (**B**) Distribution of $Q_{inter13}$ of heterotrimeric PCNA at different salt concentrations, as well as heterotrimeric PCNA without charges. (**C**) Distribution of distance between PCNA1 and PCNA3 at different salt concentrations, as well as without charges. This distance is 0.625 nm in 2HII (shown with black dashed line). (**D**) Mean salt bridge number (with standard deviation) between PCNA1 and PCNA3 at different salt concentrations. (**E**) Comparison between ring-open (middle, blue) and ring-closed (left, yellow) states of heterotrimeric PCNA. According to our simulation results, ring-open PCNA mainly adopts out-of-plane, left-hand spiral geometry.

charge, Figure 7B). By calculating the distance between the center of mass of residues involved in native contacts at the PCNA1:PCNA3 interface at varying ionic strengths, we observed that the distance of the PCNA1:PCNA3 interface lengthens as salt concentration increases (Figure 7C) and is greatest when all charges are eliminated (i.e. no attractive electrostatic forces) (no charge, Figure 7C). Our simulation also reveals that as ionic strength is increased from 10 to 500 mM, the mean number of salt bridges in the SBM decrease as interacting charges become shielded (Figure 7D), which provides a basis for the experimentally observed increases in k_{open} (Table 1) and the population of ring-open PCNA conformer as salt concentration is increased (Figures 3, 5 and 7). Taken together, our molecular dynamic simulation suggests that the proportion of ring-open PCNA conformer is dependent on ionic strength. Notably, most configurations of *Sso* PCNA from our simulation open out-of-plane with an unexpected left-hand geometry (Figure 7E).

DISCUSSION

Replication and repair of DNA are critical for cell functioning, survival, and proliferation. Accordingly, these complex processes are executed and tightly regulated *in vivo* by a host of enzymes and protein cofactors, including the sliding DNA clamp, PCNA. This ring-shaped molecule encircles DNA to serve as a processivity factor for replicative DNA polymerases, but has also been implicated as a protein scaffold upon which DNA replication and repair components assemble. As PCNA is often localized at the replication fork, any complications that arise during DNA replication, such as DNA damage or replication fork stalling, can be efficiently resolved by applicable enzymes recruited to PCNA. Structures of sliding DNA clamps from all three domains of life show a ring-closed conformation, suggesting that a ring-closed→ring-open conformational change is necessary for PCNA loading onto DNA. Indeed, RFC is known to pry open the closed PCNA ring for efficient loading onto DNA at primer/template junctions. Consistently, a structure of gp45 clamp from T4 bacteriophage was solved in a ring-open conformation only when in complex with the gp62/gp44 clamp loader and DNA (27,28,77). Similarly, a low resolution (12 Å) cryo-electron microscopy structure of archaeal PCNA in complex with RFC and DNA from *Pyrococcus furiosus* also reveals out-of-plane ring-opening (78). However, biochemical and computational evidence suggest that sliding DNA clamps may sample ring-open and ring-closed conformations (29,79), even in the absence of their respective clamp loaders, despite the aforementioned structural data. In fact, the ring-open conformation of gp45 was shown to dominate in solution by fluorescence spectroscopy (29), while only the ring-closed structure (in the presence of clamp loader) could be solved by X-ray crystallography (30). For this reason, it was previously hypothesized that crystallization conditions may in fact artificially select for the ring-closed conformation of sliding DNA clamps (79). Here, using smFRET, IM-MS, and SBM molecular dynamic simulations, we show that *Sso* PCNA exists in equilibrium between ring-open and ring-closed conformations that are sensitive to ionic strength. To our knowledge, these data are the first to demonstrate passive ring-opening and ring-closing of a sliding DNA clamp in real-time. Importantly, these dynamic conformational transitions may be significant for regulating protein-protein and protein-DNA interactions mediated by PCNA during DNA replication and repair.

The opening of sliding DNA clamps by clamp loader assemblies (i.e. gp62/gp44 in T4 bacteriophage, γ-complex in *E. coli*, RFC in archaea and eukaryotes) has been structurally and biochemically evaluated to reveal a largely conserved mechanism (80). While in complex with ATP, clamp loaders first bind and then open sliding DNA clamps. Next, this complex binds to the primer-template junction of DNA

which activates ATP hydrolysis by the clamp loader. ATP hydrolysis results in the closure of the sliding DNA clamp and dissociation of the clamp loader from the complex. While it is suspected that ATP binding to the clamp loader permits the forcible opening of the DNA clamp, an alternative hypothesis suggests that an ATP-stabilized clamp loader conformation preferentially associates with the ring-open conformation of the sliding DNA clamp (28). For the first time, our smFRET analysis has provided direct evidence for dynamic interconversion of PCNA between ring-open and ring-closed conformations (Figure 2) which supports the latter hypothesis for RFC-catalyzed clamp opening (the ATP-stabilized clamp loader associates with the ring-open PCNA). While ensemble FRET has been previously utilized to investigate the conformations of sliding DNA clamps (29,81–84), these studies could only report on the average behavior of clamp molecules. In contrast, smFRET is not constrained by ensemble averaging to permit dynamic visualization of individual molecules. Here, we surface-immobilized PCNA that was simultaenously labeled with Cy3 and Cy5 at positions sensitive to ring-opening and ring-closing at the PCNA1:PCNA3 interface for wide-field smFRET imaging (Figure 1). Based on the observed, apparent FRET efficiencies for the high- and low-FRET states (∼0.80 and 0.55, respectively) (Figures 2 and 3), as well as the Förster radius for Cy3–Cy5 (∼54 Å) (56,57), the distance change between the ring-closed and ring-open PCNA conformers is roughly 10 Å. This distance is consistent with in-plane ring-opening of ∼5–9 Å observed structurally for gp45 and archaeal PCNA in complex with their respective clamp loaders and DNA (28,78). This supports the notion that single-stranded DNA is first passed through the open ring, followed by PCNA ring-closing and subsequent sliding to the double-stranded primer-template junction, rather than additional ring-opening to permit passage of the wider double-stranded DNA (∼20 Å) (28,78). Notably, while proper data corrections are necessary to measure the absolute inter-fluorophore distance of the low- and high-FRET states, the ∼10 Å difference estimated above is a reasonable approximation as both the low-(0.40–0.60, center = 0.55) and high-(0.60–0.90, center = 0.80) FRET distributions fall squarely in the linear region of the distance-dependency of FRET efficiency for the Cy3–Cy5 pair (Supplementary Figure S3). Our molecular dynamic simulations revealed that most ring-open configurations sampled by PCNA were out-of-plane with left-hand geometry (Figure 7E). This result is consistent with previous computational reports (79,85,86) which revealed that PCNA (including yeast and human PCNA (86)) is not biased towards right-handed spiral configurations, which is in contrast to structures of DNA clamps in complex with clamp loaders (28,78,80). Accordingly, passive loading of PCNA may occur at the single-stranded region of primer-template junctions via left-hand helical geometry. Alternatively, PCNA may be stabilized in the right-hand helical geometry for DNA loading by its binding to RFC.

The novel results of our smFRET investigation were supported and cross-validated by native mass spectrometry of the wild-type *Sso* PCNA (Figure 5) and the biotinylated PCNA1–2–3 construct (Figure 6). IM-MS revealed that two conformational families existed for each construct with distinct collisional cross sections (Figures 5 and 6, Table 2). These populations are attributed to PCNA heterotrimer in either compact (ring-closed) or extended (ring-open) conformational families and are readily separated by their difference in drift time within the ion mobility cell. In order to further validate these findings we compared the experimental CCS to theoretical CCS determined from the molecular dynamics simulations performed in Figure 7. Our MD simulations were performed using coarse grained (C alpha only) structures and to the best of our knowledge, no CCS algorithm exists for CCS determination of coarse grained structures of this type. We therefore could not directly compare the values generated from the theoretical calculations to the experimental values, but could compare the trends observed. Theoretical CCS were determined using both the projection approximation (PA) and the trajectory method (TJM) algorithms in IMPACT and although the values vary significantly for these coarse grained models, the trends remain the same. Supplementary Figure S4 and Table S1 summarize the theoretical CCS results for the wild-type PCNA. As expected, the ring-closed form is more compact than the ring-open form with the average percentage difference in CCS between the two forms being 2.1%. This is in line with, although smaller than, our experimental observations of the wild-type PCNA heterotrimer in which an average 4.7% difference between the two conformational families was observed. It has been previously reported that ring complexes can undergo compaction on transfer into the gas-phase (87), which could in part explain the larger percentage difference between the two conformational families observed experimentally. Interestingly, although the absolute values are significantly different for PA and TJM, the percentage difference calculated between the two conformational families is very similar, 2.1% and 2.2% respectively.

Furthermore, the intensity of each conformational ensemble was shown to be sensitive to the concentration of mixed acetate salts (Figure 6), with higher concentrations favoring the extended conformer. The IM-MS data at different mixed acetate salt concentrations agreed with the observed influence of increasing NaCl concentrations on the proportions of FRET events at high and low efficiencies (Figure 3) and our molecular dynamic simulations (Figure 7), with low ionic strength favoring the closed PCNA conformation and high ionic strength favoring the ring-open PCNA conformation. Moreover, dwell time analysis (Figure 4) of the high- and low-FRET events yielded transitions rates for ring-closed→ring-open and ring-open→ring-closed conformational changes, respectively (Table 1). As the transition kinetics (Figure 4 and Table 1) from the ring-closed conformer ($PCNA^C$, Scheme 1) to the ring-open conformer ($PCNA^O$, Scheme 1) and occupancy of the low-FRET state (Figure 3F) showed an increasing linear dependence on ionic strength, but the reverse transition (i.e. $PCNA^O \rightarrow PCNA^C$) was not sensitive to increasing ionic strength, we expanded the simple one-step mechanism for PCNA ring-opening/ring-closing (Scheme 1A) to include an additional step (Scheme 1B). Supported by our molecular dynamic simulations (Figure 7B, C, D), as native electrostatic interactions at the PCNA1:PCNA3 interface become sufficiently shielded by electrolyte ions, $PCNA^C$ is first converted to $PCNA^Z$ which

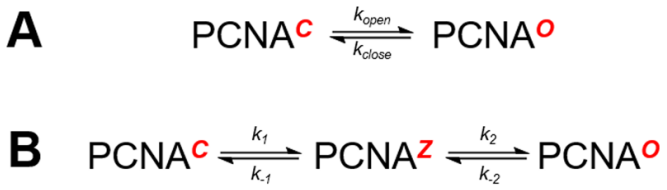

Scheme 1. (**A**) Simple mechanism of PCNA ring-opening and ring-closing. $PCNA^C$ denotes the ring-closed conformation of PCNA while $PCNA^O$ denotes the ring-open conformation. (**B**) Expanded mechanism of PCNA ring-opening and ring-closing which shows an intermediate conformation $PCNA^Z$, which represents a ring-closed form of PCNA lacking native interactions at the PCNA1:PCNA3 interface.

maintains the closed ring conformation but lacks all associated stabilizing contacts. Conversion to $PCNA^Z$ (k_1) becomes more rapid as ionic strength increases as illustrated by the slope of 1.0×10^{-4} $mM^{-1}s^{-1}$ for the best fit line to the data in Figure 4C which quantitatively describes how the ring-closed→ring-open transition rate scales with increasing NaCl concentrations. Following $PCNA^Z$ formation, conformational change to the ring-open state ($PCNA^O$, Scheme 1B) occurs rapidly (k_2) and is independent of salt concentrations. Thus, k_{open} in Table 1 is limited by k_1. During the reverse transition from $PCNA^O$ to $PCNA^C$, k_{-2} (0.038–0.051 s^{-1}, Table 1) describes the rate of the reverse conformational change to the closed ring conformation wherein native electrostatic contacts have not yet re-formed ($PCNA^Z$), and is independent of salt concentrations. Moreover, k-1 describes the reinstatement of native electrostatic contacts at the PCNA1:PCNA3 interface which presumably does not lead to a measurable FRET change and was not determined in our studies. Accordingly, k_{close} in Table 1 equals k_{-2}. Notably, the remaining interfaces of the PCNA heterotrimer (i.e. PCNA1:PCNA2 and PCNA2:PCNA3) have been shown to be much more charge-charge compatible, as well as occupy more buried surface area, than the PCNA1:PCNA3 interface, suggesting that disruption through electrostatic shielding of native interactions at these interfaces would occur at higher ionic strengths than for the PCNA1:PCNA3 interface, as supported by our native mass spectra of the wild-type PCNA heterotrimer (Figure 5) which shows dissociation of the trimer at higher ionic strengths (23). The observed instability of the wild-type PCNA heterotrimer as buffer ionic strength is increased beyond the physiological salt concentrations which are ≤500 mM (88,89) may suggest a mechanism for PCNA subunit dissociation. Indeed, it may be that disassembly of the PCNA heterotrimer favorably occurs from the ring-open state as a result of the loss in electrostatic contacts between PCNA1 and PCNA3, which agrees with the positive correlation between the ring-open state of the PCNA heterotrimer (Figure 5D–F) and observed subunit dissociation (Figure 5A–C) at higher buffer ionic strengths. Notably, the low FRET state assigned as the ring-open conformer of covalently fused PCNA during smFRET experiments (Figures 1–3) cannot be attributed to the observed subunit dissociation of the PCNA heterotrimer at higher ionic strengths as such a dissociation event would most likely result in FRET efficiencies of <0.2 as a result of the 20 amino acid linkers between PCNA1 and PCNA2, as well as PCNA2 and PCNA3. The length of the fully-extended linker is ∼70 Å (i.e. assuming 3.5 Å per amino acid) which would result in a FRET efficiency of ≤0.17 (assuming Cy3–Cy5 $R_0 \approx 54$ Å and not including the length of a typical PCNA subunit which would result in an even lower expected FRET value, near zero) upon PCNA subunit dissociation. As a low FRET efficiency threshold of 0.2 was applied during smFRET data analysis (see Materials and Methods), such near-zero FRET efficiencies, occurring from PCNA subunit dissociation at high ionic strengths, would have been removed from the overall analysis.

The observed conformational dynamics of PCNA are supported by structural data collected for *Sso* monomeric, dimeric, and trimeric PCNA (22–24). Although the angle between each monomer in the crystal structure of the heterotrimer was determined to be 120°, the angle between PCNA1 and PCNA2 in the crystal structure of the heterodimer was determined to be 130°. Accordingly, during formation of the *Sso* heterotrimer (i.e. binding of PCNA3 to the PCNA1/PCNA2 heterodimer), a significant spring tension is introduced as PCNA1 and PCNA2 are forced to bend ∼10° to accommodate PCNA3. It is thus hypothesized that PCNA ring-opening at the PCNA1:PCNA3 interface occurs to relieve the spring tension induced by PCNA3 (23). Indeed, a structural model of PCNA3 bound to the PCNA1/PCNA2 heterodimer reveals a ∼7 Å gap between PCNA1 and PCNA3 which is consistent with the ∼10 Å distance change roughly estimated through our smFRET experiments (23). As our data reveal that PCNA can open and close even in the absence of RFC, the role of the clamp loader becomes less defined. Consistently, DNA polymerase processivity assays revealed that while *Sso* PCNA was necessary to synthesize full-length DNA product, *Sso* RFC was dispensable, suggesting that *Sso* PCNA is capable of loading to a primed M13 template in the absence of RFC (77). However, the fastest rate of DNA synthesis and greatest amount of DNA product formation was achieved in the presence of both PCNA and RFC (77). Accordingly, it seems that RFC may bind to the ring-open conformation of PCNA and guide the sliding DNA clamp to primer-template junctions of DNA substrates. Moreover, *Sso* RFC may be required to accelerate the rate of *Sso* PCNA ring-opening as the passive rate of PCNA ring-opening (k_{open}), even at the highest NaCl concentration, was only 0.13 s^{-1} (Table 1) which is considerably slower than the estimated association rate of the binary complex of RFC/PCNA to DNA (100 s^{-1}) (77). At a more physiologically relevant salt concentration (250 mM), k_{open} was determined to be even slower (0.0374 s^{-1}, Table 1) and the majority of PCNA molecules were observed in the ring-closed conformation (Figure 3B), further underlining the need for RFC to accelerate and stabilize the ring-open conformation of *Sso* PCNA for loading onto DNA. As the rate of replication fork progression in a hyperthermophilic organism such as *Sulfolobus solfataricus* is likely very fast, it is crucial that *Sso* PCNA be quickly and efficiently directed to priming sites for Okazaki fragment synthesis during lagging strand replication. Furthermore, MS data demonstrating that the wild-type *Sso* PCNA heterotrimer significantly

dissociates into monomer and dimer constituents when the ionic strength is increased to a 500 mM mixed acetate salt threshold (Figure 5) underlines the need for RFC to stabilize the PCNA heterotrimer for clamp loading.

Collectively, our interdisciplinary approach has revealed a model PCNA to be a conformationally dynamic protein. The trends in protein conformational dynamics observed in solution during our smFRET experiments are conserved in the gas phase measurements of the solution structures during our IM-MS experiments. Thus, our work further validates native mass spectrometry as an effective tool to study the dynamic motions of proteins. We are eager to apply this methodology to investigate how the observed dynamics exhibited by PCNA may contribute to clamp loading onto DNA as well as key protein-protein and protein-DNA interactions mediated by PCNA during DNA replication, DNA damage response and DNA repair.

SUPPLEMENTARY DATA

Supplementary Data are available at NAR Online.

FUNDING

National Science Foundation [MCB-1716168, PHY-76066 to Z.S., J.W.]; National Institutes of Health [GM113658 to V.H.W.]; UK Engineering and Physical Sciences Research Council (EPSRC) Doctoral Prize Fellowship awarded through the University of Manchester (to S.R.H.); National Institutes of Health Training Fellowship [T32GM008512 to A.T.R.]; National Natural Science Foundation of China [91430217 to W.T.C.]. Funding for open access charge: National Science Foundation [MCB-1716168, PHY-76066 to Z.S., J.W.]; National Institutes of Health [GM113658 to V.H.W.].

Conflict of interest statement. None declared.

REFERENCES

1. Beese,L.S., Derbyshire,V. and Steitz,T.A. (1993) Structure of DNA polymerase I Klenow fragment bound to duplex DNA. *Science*, **260**, 352–355.
2. Steitz,T.A. (1998) A mechanism for all polymerases. *Nature*, **391**, 231–232.
3. Brautigam,C.A. and Steitz,T.A. (1998) Structural and functional insights provided by crystal structures of DNA polymerases and their substrate complexes. *Curr. Opin. Struct. Biol.*, **8**, 54–63.
4. Steitz,T.A. (1999) DNA polymerases: structural diversity and common mechanisms. *J. Biol. Chem.*, **274**, 17395–17398.
5. Beard,W.A. and Wilson,S.H. (2003) Structural insights into the origins of DNA polymerase fidelity. *Structure*, **11**, 489–496.
6. Kunkel,T.A. (2004) DNA replication fidelity. *J. Biol. Chem.*, **279**, 16895–16898.
7. Joyce,C.M. and Benkovic,S.J. (2004) DNA polymerase fidelity: kinetics, structure, and checkpoints. *Biochemistry*, **43**, 14317–14324.
8. Garcia-Diaz,M. and Bebenek,K. (2007) Multiple functions of DNA polymerases. *Crit. Rev. Plant Sci.*, **26**, 105–122.
9. Dodson,M.L., Michaels,M.L. and Lloyd,R.S. (1994) Unified catalytic mechanism for DNA glycosylases. *J. Biol. Chem.*, **269**, 32709–32712.
10. Yang,W. (2008) Structure and mechanism for DNA lesion recognition. *Cell Res.*, **18**, 184–197.
11. Friedman,J.I. and Stivers,J.T. (2010) Detection of damaged DNA bases by DNA glycosylase enzymes. *Biochemistry*, **49**, 4957–4967.
12. Lehman,I.R. (1974) DNA ligase: structure, mechanism, and function. *Science*, **186**, 790–797.
13. Tomkinson,A.E., Vijayakumar,S., Pascal,J.M. and Ellenberger,T. (2006) DNA ligases: structure, reaction mechanism, and function. *Chem Rev.*, **106**, 687–699.
14. Nishino,T. and Morikawa,K. (2002) Structure and function of nucleases in DNA repair: shape, grip and blade of the DNA scissors. *Oncogene*, **21**, 9022–9032.
15. Yang,W. (2011) Nucleases: diversity of structure, function and mechanism. *Q. Rev. Biophys.*, **44**, 1–93.
16. Finger,L.D., Atack,J.M., Tsutakawa,S., Classen,S., Tainer,J., Grasby,J. and Shen,B. (2012) The wonders of flap endonucleases: structure, function, mechanism and regulation. *Sub-cell. Biochem.*, **62**, 301–326.
17. Lewis,J.S., Jergic,S. and Dixon,N.E. (2016) The E. coli DNA replication fork. *Enzymes*, **39**, 31–88.
18. Zhang,D. and O'Donnell,M. (2016) The eukaryotic replication machine. *Enzymes*, **39**, 191–229.
19. Noble,E., Spiering,M.M. and Benkovic,S.J. (2015) Coordinated DNA replication by the bacteriophage T4 replisome. *Viruses*, **7**, 3186–3200.
20. Indiani,C. and O'Donnell,M. (2006) The replication clamp-loading machine at work in the three domains of life. *Nat. Rev. Mol. Cell Biol.*, **7**, 751–761.
21. Dionne,I., Nookala,R.K., Jackson,S.P., Doherty,A.J. and Bell,S.D. (2003) A heterotrimeric PCNA in the hyperthermophilic archaeon Sulfolobus solfataricus. *Mol. Cell*, **11**, 275–282.
22. Williams,G.J., Johnson,K., Rudolf,J., McMahon,S.A., Carter,L., Oke,M., Liu,H., Taylor,G.L., White,M.F. and Naismith,J.H. (2006) Structure of the heterotrimeric PCNA from Sulfolobus solfataricus. *Acta Crystallogr. F*, **62**, 944–948.
23. Hlinkova,V., Xing,G., Bauer,J., Shin,Y.J., Dionne,I., Rajashankar,K.R., Bell,S.D. and Ling,H. (2008) Structures of monomeric, dimeric and trimeric PCNA: PCNA-ring assembly and opening. *Acta Crystallogr. D*, **64**, 941–949.
24. Pascal,J.M., Tsodikov,O.V., Hura,G.L., Song,W., Cotner,E.A., Classen,S., Tomkinson,A.E., Tainer,J.A. and Ellenberger,T. (2006) A flexible interface between DNA ligase and PCNA supports conformational switching and efficient ligation of DNA. *Mol. Cell*, **24**, 279–291.
25. Dore,A.S., Kilkenny,M.L., Jones,S.A., Oliver,A.W., Roe,S.M., Bell,S.D. and Pearl,L.H. (2006) Structure of an archaeal PCNA1-PCNA2-FEN1 complex: elucidating PCNA subunit and client enzyme specificity. *Nucleic Acids Res.*, **34**, 4515–4526.
26. Xing,G., Kirouac,K., Shin,Y.J., Bell,S.D. and Ling,H. (2009) Structural insight into recruitment of translesion DNA polymerase Dpo4 to sliding clamp PCNA. *Mol. Microbiol.*, **71**, 678–691.
27. Dionne,I., Brown,N.J., Woodgate,R. and Bell,S.D. (2008) On the mechanism of loading the PCNA sliding clamp by RFC. *Mol. Microbiol.*, **68**, 216–222.
28. Kelch,B.A., Makino,D.L., O'Donnell,M. and Kuriyan,J. (2011) How a DNA polymerase clamp loader opens a sliding clamp. *Science*, **334**, 1675–1680.
29. Millar,D., Trakselis,M.A. and Benkovic,S.J. (2004) On the solution structure of the T4 sliding clamp (gp45). *Biochemistry*, **43**, 12723–12727.
30. Moarefi,I., Jeruzalmi,D., Turner,J., O'Donnell,M. and Kuriyan,J. (2000) Crystal structure of the DNA polymerase processivity factor of T4 bacteriophage. *J. Mol. Biol.*, **296**, 1215–1223.
31. Fairhead,M. and Howarth,M. (2015) Site-specific biotinylation of purified proteins using BirA. *Methods Mol. Biol.*, **1266**, 171–184.
32. Studier,F.W. (2005) Protein production by auto-induction in high density shaking cultures. *Protein Expression Purif.*, **41**, 207–234.
33. O'Callaghan,C.A., Byford,M.F., Wyer,J.R., Willcox,B.E., Jakobsen,B.K., McMichael,A.J. and Bell,J.I. (1999) BirA enzyme: production and application in the study of membrane receptor-ligand interactions by site-specific biotinylation. *Anal. Biochem.*, **266**, 9–15.
34. Selvin,P.R. and Ha,T. (2008) *Single-molecule Techniques: A Laboratory Manual*. Cold Spring Harbor Laboratory Press, NY.
35. Maxwell,B.A. and Suo,Z. (2013) Single-molecule investigation of substrate binding kinetics and protein conformational dynamics of a B-family replicative DNA polymerase. *J. Biol. Chem.*, **288**, 11590–11600.
36. Raper,A.T., Gadkari,V.V., Maxwell,B.A. and Suo,Z. (2016) Single-molecule investigation of response to oxidative DNA damage by a Y-family DNA polymerase. *Biochemistry*, **55**, 2187–2196.

37. Chandradoss,S.D., Haagsma,A.C., Lee,Y.K., Hwang,J.H., Nam,J.M. and Joo,C. (2014) Surface passivation for single-molecule protein studies. *J. Visual. Exp.: JoVE.*, **86**, e50549.
38. Rasnik,I., McKinney,S.A. and Ha,T. (2006) Nonblinking and long-lasting single-molecule fluorescence imaging. *Nat. Methods*, **3**, 891–893.
39. Zhou,M., Huang,C. and Wysocki,V.H. (2012) Surface-induced dissociation of ion mobility-separated noncovalent complexes in a quadrupole/time-of-flight mass spectrometer. *Anal. Chem.*, **84**, 6016–6023.
40. Bush,M.F., Hall,Z., Giles,K., Hoyes,J., Robinson,C.V. and Ruotolo,B.T. (2010) Collision cross sections of proteins and their complexes: a calibration framework and database for gas-phase structural biology. *Anal. Chem.*, **82**, 9557–9565.
41. Noel,J.K., Whitford,P.C., Sanbonmatsu,K.Y. and Onuchic,J.N. (2010) SMOG@ctbp: simplified deployment of structure-based models in GROMACS. *Nucleic Acids Res.*, **38**, W657–W661.
42. Clementi,C., Nymeyer,H. and Onuchic,J.N. (2000) Topological and energetic factors: what determines the structural details of the transition state ensemble and "en-route" intermediates for protein folding? An investigation for small globular proteins. *J. Mol. Biol.*, **298**, 937–953.
43. Noel,J.K., Whitford,P.C. and Onuchic,J.N. (2012) The shadow map: a general contact definition for capturing the dynamics of biomolecular folding and function. *J. Phys. Chem. B*, **116**, 8692–8702.
44. Miyazawa,S. and Jernigan,R.L. (1996) Residue-residue potentials with a favorable contact pair term and an unfavorable high packing density term, for simulation and threading. *J. Mol. Biol.*, **256**, 623–644.
45. Cho,S.S., Levy,Y. and Wolynes,P.G. (2009) Quantitative criteria for native energetic heterogeneity influences in the prediction of protein folding kinetics. *Proc. Natl. Acad. Sci. U.S.A.*, **106**, 434–439.
46. Azia,A. and Levy,Y. (2009) Nonnative electrostatic interactions can modulate protein folding: molecular dynamics with a grain of salt. *J. Mol. Biol.*, **393**, 527–542.
47. Givaty,O. and Levy,Y. (2009) Protein sliding along DNA: dynamics and structural characterization. *J. Mol. Biol.*, **385**, 1087–1097.
48. Chu,X., Wang,Y., Gan,L., Bai,Y., Han,W., Wang,E. and Wang,J. (2012) Importance of electrostatic interactions in the association of intrinsically disordered histone chaperone Chz1 and histone H2A.Z-H2B. *PLoS Comput. Biol.*, **8**, e1002608.
49. Wang,Y., Gan,L., Wang,E. and Wang,J. (2013) Exploring the dynamic functional landscape of Adenylate kinase modulated by substrates. *J. Chem. Theory Comput.*, **9**, 84–95.
50. Hess,B., Kutzner,C., van der Spoel,D. and Lindahl,E. (2008) GROMACS 4: Algorithms for highly efficient, load-balanced, and scalable molecular simulation. *J. Chem. Theory Comput.*, **4**, 435–447.
51. Hess,B., Bekker,H., Berendsen,H.J.C. and Fraaije,J.G.E.M. (1997) LINCS: a linear constraint solver for molecular simulations. *J. Comput. Chem.*, **18**, 1463–1472.
52. Marklund,E.G., Degiacomi,M.T., Robinson,C.V., Baldwin,A.J. and Benesch,J.L. (2015) Collision cross sections for structural proteomics. *Structure*, **23**, 791–799.
53. Lehmann,A.R., Niimi,A., Ogi,T., Brown,S., Sabbioneda,S., Wing,J.F., Kannouche,P.L. and Green,C.M. (2007) Translesion synthesis: Y-family polymerases and the polymerase switch. *DNA Repair*, **6**, 891–899.
54. Lovett,S.T. (2007) Polymerase switching in DNA replication. *Mol. Cell*, **27**, 523–526.
55. Heltzel,J.M., Maul,R.W., Scouten Ponticelli,S.K. and Sutton,M.D. (2009) A model for DNA polymerase switching involving a single cleft and the rim of the sliding clamp. *Proc. Natl. Acad. Sci. U.S.A.*, **106**, 12664–12669.
56. Lee,S., Lee,J. and Hohng,S. (2010) Single-molecule three-color FRET with both negligible spectral overlap and long observation time. *PLoS One*, **5**, e12270.
57. Dietrich,A., Buschmann,V., Muller,C. and Sauer,M. (2002) Fluorescence resonance energy transfer (FRET) and competing processes in donor-acceptor substituted DNA strands: a comparative study of ensemble and single-molecule data. *J. Biotechnol.*, **82**, 211–231.
58. Roy,R., Hohng,S. and Ha,T. (2008) A practical guide to single-molecule FRET. *Nat. Methods*, **5**, 507–516.
59. Sharon,M. and Robinson,C.V. (2007) The role of mass spectrometry in structure elucidation of dynamic protein complexes. *Annu. Rev. Biochem.*, **76**, 167–193.
60. Marcoux,J. and Robinson,C.V. (2013) Twenty years of gas phase structural biology. *Structure*, **21**, 1541–1550.
61. Benesch,J.L., Ruotolo,B.T., Simmons,D.A. and Robinson,C.V. (2007) Protein complexes in the gas phase: technology for structural genomics and proteomics. *Chem. Rev.*, **107**, 3544–3567.
62. Uetrecht,C., Versluis,C., Watts,N.R., Wingfield,P.T., Steven,A.C. and Heck,A.J. (2008) Stability and shape of hepatitis B virus capsids in vacuo. *Angew. Chem.*, **47**, 6247–6251.
63. Dyachenko,A., Gruber,R., Shimon,L., Horovitz,A. and Sharon,M. (2013) Allosteric mechanisms can be distinguished using structural mass spectrometry. *Proc. Natl. Acad. Sci. U.S.A.*, **110**, 7235–7239.
64. Uetrecht,C., Rose,R.J., van Duijn,E., Lorenzen,K. and Heck,A.J. (2010) Ion mobility mass spectrometry of proteins and protein assemblies. *Chem. Soc. Rev.*, **39**, 1633–1655.
65. Konijnenberg,A., Butterer,A. and Sobott,F. (2013) Native ion mobility-mass spectrometry and related methods in structural biology. *Biochim. Biophys. Acta*, **1834**, 1239–1256.
66. Jenner,M., Ellis,J., Huang,W.C., Lloyd Raven,E., Roberts,G.C. and Oldham,N.J. (2011) Detection of a protein conformational equilibrium by electrospray ionisation-ion mobility-mass spectrometry. *Angew. Chem.*, **50**, 8291–8294.
67. Harvey,S.R., Porrini,M., Konijnenberg,A., Clarke,D.J., Tyler,R.C., Langridge-Smith,P.R., MacPhee,C.E., Volkman,B.F. and Barran,P.E. (2014) Dissecting the dynamic conformations of the metamorphic protein lymphotactin. *J. Phys. Chem. B*, **118**, 12348–12359.
68. Hall,Z., Politis,A., Bush,M.F., Smith,L.J. and Robinson,C.V. (2012) Charge-state dependent compaction and dissociation of protein complexes: insights from ion mobility and molecular dynamics. *J. Am. Chem. Soc.*, **134**, 3429–3438.
69. Zhou,M., Dagan,S. and Wysocki,V.H. (2013) Impact of charge state on gas-phase behaviors of noncovalent protein complexes in collision induced dissociation and surface induced dissociation. *Analyst*, **138**, 1353–1362.
70. Xiao,Q., Zhang,F., Nacev,B.A., Liu,J.O. and Pei,D. (2010) Protein N-terminal processing: substrate specificity of Escherichia coli and human methionine aminopeptidases. *Biochemistry*, **49**, 5588–5599.
71. Quintyn,R.S., Zhou,M., Yan,J. and Wysocki,V.H. (2015) Surface-induced dissociation mass spectra as a tool for distinguishing different structural forms of gas-phase multimeric protein complexes. *Anal. Chem.*, **87**, 11879–11886.
72. Ganguly,D. and Chen,J. (2011) Topology-based modeling of intrinsically disordered proteins: balancing intrinsic folding and intermolecular interactions. *Proteins*, **79**, 1251–1266.
73. Ganguly,D., Otieno,S., Waddell,B., Iconaru,L., Kriwacki,R.W. and Chen,J. (2012) Electrostatically accelerated coupled binding and folding of intrinsically disordered proteins. *J. Mol. Biol.*, **422**, 674–684.
74. Law,S.M., Gagnon,J.K., Mapp,A.K. and Brooks,C.L. 3rd (2014) Prepaying the entropic cost for allosteric regulation in KIX. *Proc. Natl. Acad. Sci. U.S.A.*, **111**, 12067–12072.
75. Lu,Q., Lu,H.P. and Wang,J. (2007) Exploring the mechanism of flexible biomolecular recognition with single molecule dynamics. *Phys. Rev. Lett.*, **98**, 128105.
76. Turjanski,A.G., Gutkind,J.S., Best,R.B. and Hummer,G. (2008) Binding-induced folding of a natively unstructured transcription factor. *PLoS Comput. Biol.*, **4**, e1000060.
77. Bauer,R.J., Wolff,I.D., Zuo,X., Lin,H.K. and Trakselis,M.A. (2013) Assembly and distributive action of an archaeal DNA polymerase holoenzyme. *J. Mol. Biol.*, **425**, 4820–4836.
78. Miyata,T., Suzuki,H., Oyama,T., Mayanagi,K., Ishino,Y. and Morikawa,K. (2005) Open clamp structure in the clamp-loading complex visualized by electron microscopic image analysis. *Proc. Natl. Acad. Sci. U.S.A.*, **102**, 13795–13800.
79. Oakley,A.J. (2016) Dynamics of open DNA sliding clamps. *PLoS One*, **11**, e0154899.
80. Kelch,B.A., Makino,D.L., O'Donnell,M. and Kuriyan,J. (2012) Clamp loader ATPases and the evolution of DNA replication machinery. *BMC Biol.*, **10**, 34.
81. Alley,S.C., Shier,V.K., Abel-Santos,E., Sexton,D.J., Soumillion,P. and Benkovic,S.J. (1999) Sliding clamp of the bacteriophage T4

polymerase has open and closed subunit interfaces in solution. *Biochemistry*, **38**, 7696–7709.
82. Trakselis,M.A., Alley,S.C., Abel-Santos,E. and Benkovic,S.J. (2001) Creating a dynamic picture of the sliding clamp during T4 DNA polymerase holoenzyme assembly by using fluorescence resonance energy transfer. *Proc. Natl. Acad. Sci. U.S.A.*, **98**, 8368–8375.
83. Zhuang,Z., Yoder,B.L., Burgers,P.M. and Benkovic,S.J. (2006) The structure of a ring-opened proliferating cell nuclear antigen-replication factor C complex revealed by fluorescence energy transfer. *Proc. Natl. Acad. Sci. U.S.A.*, **103**, 2546–2551.
84. Kumar,R., Nashine,V.C., Mishra,P.P., Benkovic,S.J. and Lee,T.H. (2010) Stepwise loading of yeast clamp revealed by ensemble and single-molecule studies. *Proc. Natl. Acad. Sci. U.S.A.*, **107**, 19736–19741.
85. Adelman,J.L., Chodera,J.D., Kuo,I.F., Miller,T.F. 3rd and Barsky,D. (2010) The mechanical properties of PCNA: implications for the loading and function of a DNA sliding clamp. *Biophys. J.*, **98**, 3062–3069.
86. Kazmirski,S.L., Zhao,Y., Bowman,G.D., O'Donnell,M. and Kuriyan,J. (2005) Out-of-plane motions in open sliding clamps: molecular dynamics simulations of eukaryotic and archaeal proliferating cell nuclear antigen. *Proc. Natl. Acad. Sci. U.S.A.*, **102**, 13801–13806.
87. Ruotolo,B.T., Giles,K., Campuzano,I., Sandercock,A.M., Bateman,R.H. and Robinson,C.V. (2005) Evidence for macromolecular protein rings in the absence of bulk water. *Science*, **310**, 1658–1661.
88. Fagerbakke,K.M., Norland,S. and Heldal,M. (1999) The inorganic ion content of native aquatic bacteria. *Can. J. Microbiol.*, **45**, 304–311.
89. Ando,T. and Skolnick,J. (2010) Crowding and hydrodynamic interactions likely dominate in vivo macromolecular motion. *Proc. Natl. Acad. Sci. U.S.A.*, **107**, 18457–18462.